OATAO
Open Archive Toulouse Archive Ouverte

Open Archive Toulouse Archive Ouverte

OATAO is an open access repository that collects the work of Toulouse researchers and makes it freely available over the web where possible

This is an author's version published in: http://oatao.univ-toulouse.fr/24174

Official URL:

https://doi.org/10.1016/j.ijheatmasstransfer.2019.118521

Any correspondence concerning this service should be sent to the repository administrator: tech-oatao@listes-diff.inp-toulouse.fr

Direct numerical simulation of nucleate boiling in zero gravity conditions

A. Urbano *, S. Tanguy, C. Colin

Institut de Mécanique des Fluides de Toulouse (IMFT), Université de Toulouse, CNRS, Toulouse, France

ABSTRACT

Understanding and controlling nucleate pool boiling phenomena in zero gravity conditions is fundamental for space applications. An analytical model for the equilibrium radius reached by a bubble nucleated in sub-cooled conditions is established in this work and verified numerically. Indeed, direct numerical simulations of two phase flows conjugated with the heat conduction in the solid wall are carried out in order to verify and correct the analytical model. Fine grids, with cells size of the order of the micron, are mandatory in order to capture the subtle equilibrium between condensation and evaporation that characterises stationary conditions. This has been possible thanks to the house made solver $\mathcal{DIVA}$, validated for nucleate pool boiling simulations, and that permits to carry out parallel numerical simulations. Results show that the equilibrium radius of the bubble is a function of the thermal gradient, of the Jakob numbers associated with condensation and evaporation and of the apparent contact angle. The analysis of the thermal field is carried out and an interpretation of the physical processes that characterise the equilibrium is given. In addition, useful information on the heat transfer behaviour, reported in terms of Nu numbers, completes the work.

1. Introduction

Cryogenics propellants are stored in a liquid state in space tanks, at a temperature which is only a few degrees smaller than the saturation temperature. Even low heat loads could induce nucleate boiling. The consequences are an increase in the pressure and the risk of pumping vapour in the feed system. It is thus very important to be able to predict and to control the phenomenon. Nucleate boiling in micro-gravity conditions is actually a topic of large scientific interest, and a number of questions remain unanswered. For instance there are open questions on the quantitative impact of the gravity level on the critical heat flux and more in general on the heat transfer behaviour [1,2]. Moreover, the impact of wall superheat and wetting properties, that have been largely investigated in normal gravity conditions, are not clearly understood in micro-gravity conditions [3,4]. Therefore basic studies, dealing with single bubbles, are required to improve our understanding. As a matter of fact, in terrestrial gravity conditions, complex experiments with long observation times are possible. On the other hand, things become much more complicated if micro-gravity conditions are searched. Most of the experiments in

micro-gravity are carried out using drop towers, sounding rockets [5] or during parabolic flights [6,7]. However, the drawbacks of these methodologies are a short observation time and continuously varying gravity conditions. The gravity acceleration never reaches a zero value, but typically a minimum value that varies between 10^{-2} et $10^{-6} g$ [8,9,7,10,2]. To achieve longer times and lower gravity levels down to $10^{-7} g$, orbital flights must be considered, onboard a space station for instance, but these experiments are rare and expensive [11,3].

Numerical solvers based either on fundamental conservation equations [12,13] or Lattice Boltzmann equations [14,15] can be used to simulate nucleate boiling. In the present paper, we will focus on the first class of numerical solvers. From a numerical point of view, varying or suppressing the gravity acceleration does not present any immediate constraint. However, the requirements in terms of resolutions (small grid cells size) in order to achieve converged results, the long simulation times and the complexity of the phenomenon strongly impact the cost of the problem (long computational time) and its difficulty [16,13,17]. This could explain the low number of numerical works available in the literature dealing with direct numerical simulation, of nucleate boiling in microgravity conditions.

The goal of the present research is to bring insight into the physics of nucleate boiling in zero gravity conditions, making use of

---
* Corresponding author.
  E-mail address: annafederica.urbano@isae-supaero.fr (A. Urbano).

direct numerical simulations, and to deduce useful informations to be used in tanks management. Specifically, the work focuses on the problem of one bubble nucleated in sub-cooled and zero gravity conditions. Experiments have shown that a steady boiling could be reached for low sub-cooling levels (smaller than 10 K) [1,9] and our objective is to quantitatively evaluate the impact of sub-cooling, wall superheat and wetting properties on the bubble dimension and conjugate heat transfer. It it worth to mention that it has been experimentally observed that the presence of non condensable gases could strongly affect the phenomenon by inducing thermocapillary convection [18,8,10]. However, in the present work we wish to focus on the impact of the temperatures and the wetting properties only, and therefore a one species vapour-liquid system will be considered. First, an analytical model for the equilibrium radius is presented. Then, the numerical solver used to carried out direct numerical simulations in axisymmetric configurations is presented. Attention is given to the appropriate-ness of the selected numerical schemes, to the boundary condi-tions and to the selection of a grid cell size that allows to achieve converged solutions. With the selected configuration, direct numerical simulations are carried out in order to verify the analyt-ical model. Eventually, the impacts of the Jakob numbers and of the contact angle on the heat transfer are investigated.

2. Equilibrium radius of a bubble nucleated in zero gravity conditions

The goal of the analytical reasoning here described is to under-stand what are the impacts of the temperatures and of the contact angle over the equilibrium radius reached by a bubble which is nucleated in a partly subcooled liquid pool, in zero gravity condi-tions. We will consider low sub-cooling levels, for which experi-ments have shown that a stable boiling is possible [9].

Let us consider a box of height L filled with a liquid, which is schematically represented with a 2D view in Fig. 1. A cylindrical coordinate system (r, φ, z) is defined and we assume an axisym-metric configuration with z being the symmetry axis (the azi-muthal angle φ is not represented in Fig. 1). Two opposite walls of the box are kept isothermal: the wall at $z = 0$ is at a temperature T_w greater than the saturation temperature T_{sat} ($T_w > T_{sat}$), and the wall at $z = L$ is at a subcooled temperature $T_{sub} < T_{sat}$. The other

walls are adiabatic. If the gravity acceleration is zero, in stationary conditions we can expect a linear thermal field to establish by con-duction between T_w and T_{sub}:

$$T(z) = T_w + \frac{T_{sub} - T_w}{L} z. \tag{1}$$

In these conditions a nucleated bubble at the hot wall initially grows without detaching (because there is no buoyancy force). When the bubble is big enough to reach the subcooled region, its growth is slowed down because the bubble partly condensates. We can reasonably guess that the bubble will reach an equilibrium spherical shape when the mass flow rate leaving the bubble by con-densation will compensate the mass flow rate inflating the bubble by evaporation, which can be mathematically expressed with an integral over the surface of the bubble S_b:

$$\int_{S_b} \dot{m} dS = 0, \tag{2}$$

where $\dot{m}$ is the specific phase change mass flow rate which is given by the jump relation:

$$\dot{m} = \frac{\left[-k \nabla T . \overrightarrow{n} \right]_\Gamma}{L_{vap}} \simeq \frac{k_l \nabla T_l . \overrightarrow{n}}{L_{vap}}. \tag{3}$$

The operator $[.]_\Gamma$ indicates the jump across the interface Γ and is defined by:

$$[f]_\Gamma = f_v - f_l, \tag{4}$$

with the subscripts l and v referring respectively to the liquid and vapour phases. L_{vap} is the latent heat of vaporisation, k is the ther-mal conductivity and $\overrightarrow{n}$ is the normal vector at the interface, point-ing towards the liquid phase. The right hand side of Eq. (3) comes out from neglecting the product $k \nabla T$ in the vapour with respect to the same product in the liquid ($k_v < k_l$ and $\nabla T_v < \nabla T_l$). The equi-librium radius R_b can be deduced by analytically solving Eq. (2). A spherical coordinate system (R, θ, φ) is defined, with the origin in the center of the bubble (see Fig. 1). In this reference frame, the sur-face integral of Eq. (2) can be expressed with a linear integral, con-sidering that $dS = 2\pi R^2 \cos \theta d\theta$ (with the axisymmetric assumption):
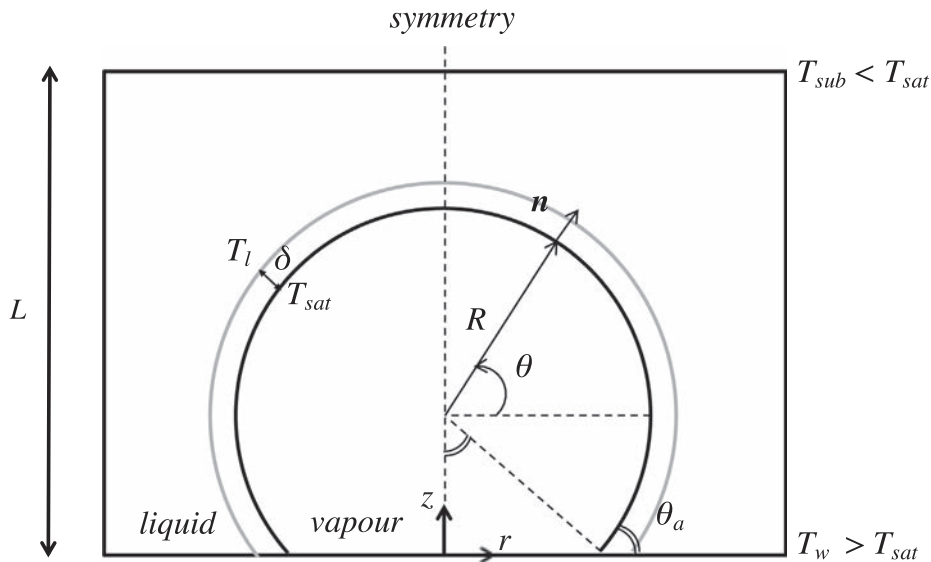

Fig. 1. Schematic of the problem and reference frame used to establish the analytical model.

$$\dot{m} = \int_{-\frac{\pi}{2}+\theta_a}^{\frac{\pi}{2}} \frac{k_l \nabla T_l \cdot \vec{n}}{L_{vap}} 2\pi R^2 \cos\theta d\theta, \qquad (5)$$

where θ_a is the apparent contact angle (outside the micro region, see appendix in [19] for more details). The integral of Eq. (5) is null when the equilibrium radius is reached, that is for $R = R_b$. The interface of the bubble is at the saturation temperature T_{sat} in agreement with the second law of thermodynamics for a pure liquid-vapour system at local thermodynamic equilibrium. There is a thermal boundary layer of thickness δ around the bubble in which the temperature varies from T_{sat} at the interface to the liquid temperature $T(z)$ outside the boundary layer (see Fig. 1). We assume that δ is constant along the bubble surface, which implies that it does not depend on the local temperature. Actually, using Eq. (1), we can express the temperature in the liquid along the bubble interface, which has a radius R, as a function of θ:

$$T(\theta) = T_w + \frac{T_{sub} - T_w}{L}(R\cos(\theta_a) + R\sin(\theta)). \qquad (6)$$

The corresponding normal thermal gradient between the interface and the liquid, across the thermal boundary layer is:

$$\nabla T_l \cdot \vec{n} = \frac{1}{\delta}(T(\theta) - T_{sat}). \qquad (7)$$

More details are reported in Appendix A. Finally, using Eqs. (7) and (6) to express Eq. (5) and requiring it equals zero, a relation for the equilibrium radius R_b is found:

$$\frac{R_b}{L} = \left[\left(1 + \frac{Ja_c}{Ja_e}\right)\cos\theta_a + \frac{\sin^2\theta_a}{2(1 + \cos\theta_a)}\right]^{-1}. \qquad (8)$$

The ratio between Ja_c and Ja_e, which are the Jakob numbers associated with condensation and evaporation, corresponds to the ratio between sub-cooling and wall superheat:

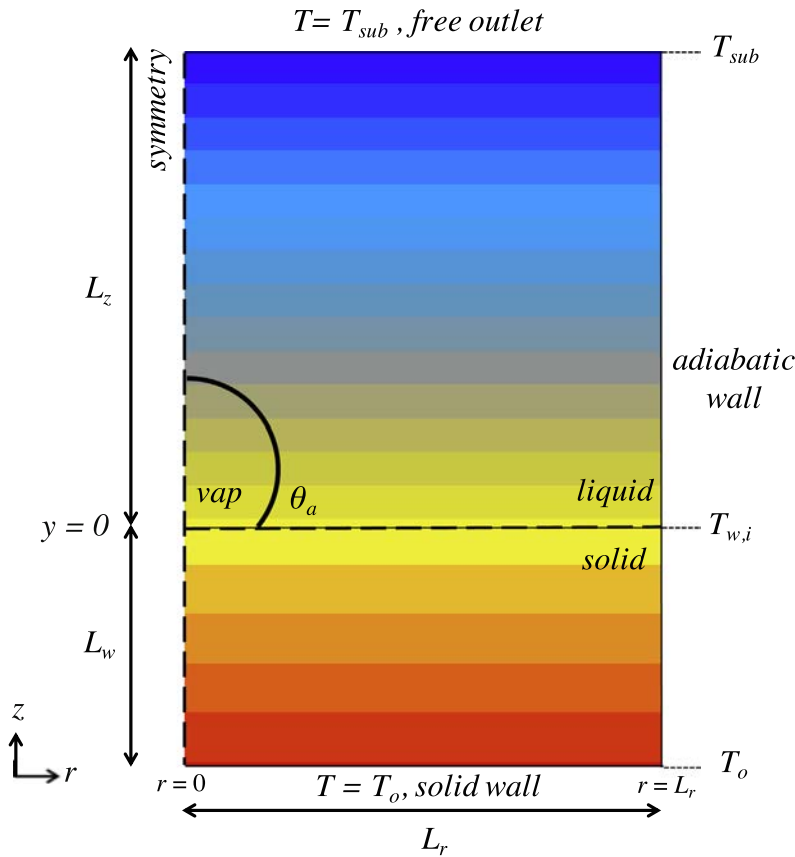$$\frac{Ja_c}{Ja_e} = \frac{T_{sat} - T_{sub}}{T_w - T_{sat}}. \qquad (9)$$

Fig. 2. Computational domain, initial conditions (temperature field and initial vapour seed) and boundary conditions. Size of the seed not in scale.

Table 1
Thermophysical properties for water in liquid and gas phase, at $p = 1.01$ bar, with $T_{sat} = 373.12$ K, and for the solid wall material (plastic similar to PA66).

	ρ [kg/m^3]	μ [Pa s]	k [W/K/m]	c_p [J/kg/K]	σ [N/m]	L_{vap} [J/kg]
Liquid	958	2.82×10^{-4}	0.677	4216	0.058	2.256×10^6
Vapour	0.5974	1.228×10^{-5}	0.024	2034	–	–
Solid	1.4	–	1	1500	–	–

The analytical model of Eq. (8) indicates that the equilibrium radius scales with the domain size, which imposes the temperature gradient, it is inversely proportional to the ratio Ja_c/Ja_e and it increases with the contact angle. Direct numerical simulations of single bubbles nucleated in zero gravity conditions are presented later in the paper and will permit to verify the relevance of the analytical model of Eq. (8).

3. Numerical solver

3.1. Mathematical formalism

To mathematically describe the nucleate boiling in a box in zero gravity conditions, we consider an isobaric environment and we neglect the heat produced by viscous dissipation. Therefore we assume an incompressible two-phase flow of a single component fluid which can be described by the following conservation laws, in the liquid and vapour phases, in zero gravity conditions:

$$\nabla.\vec{V} = 0, \tag{10}$$

$$\rho\frac{D\vec{V}}{Dt} = -\overrightarrow{\nabla p} + \nabla.(2\mu\mathbf{D}), \tag{11}$$

$$\rho c_p\frac{DT}{Dt} = \nabla.(k\nabla T), \tag{12}$$

where $\vec{V}$ is the velocity field, p is the pressure, T is the temperature and $\mathbf{D}$ is the deformation tensor. The thermophysical properties (conductivity k, viscosity μ and specific heat at constant pressure c_p) and the density ρ are constant in each phase. At the interface Γ, the following jump conditions (mass, momentum and energy), that account for phase change, must be satisfied:

$$\left[\vec{V}\right]_\Gamma = \dot{m}\left[\frac{1}{\rho}\right]_\Gamma\vec{n}, \tag{13}$$

$$[p]_\Gamma = \sigma\kappa + 2\left[\mu\frac{\partial V_n}{\partial n}\right]_\Gamma - \dot{m}^2\left[\frac{1}{\rho}\right]_\Gamma, \tag{14}$$

$$\left[-k\nabla T.\vec{n}\right]_\Gamma = \dot{m}L_{vap}, \tag{15}$$

where σ is the surface tension, κ denotes the local interface curvature and V_n is the velocity component in the $\vec{n}$ direction. The energy jump condition Eq. (15) has been used in Section 2, and as previously stated, it assumes that the interface is at the saturation temperature ($T_\Gamma = T_{sat}$) and we assume that T_{sat} is constant (see [20] for more details). Moreover, only single species fluids are considered. The consequence is that the surface tension σ is constant and therefore Marangoni convection effects, which could be induced by the presence of non condensable species in the gas, are neglected.

Finally, the above system equation for the fluid must be coupled with the energy conservation in the heated solid wall:

$$\rho_w c_{p,w}\frac{\partial T}{\partial t} = k_w\Delta T, \tag{16}$$

where $\rho_w, c_{p,w}$ and k_w are constant in the solid. At the solid/fluid interface, the requirements will be an equality of the heat fluxes and a continuity of the temperature.

3.2. Numerical schemes

The above mathematical formalism is implemented in the in house code $\mathcal{DIVA}$ that has been used for the direct numerical simulations presented in this paper. The interface motion is computed with the Level Set method [21] making use of a preserving distance algorithm [22]. The sharp description of the flow across the interface is made possible thanks to the Ghost Fluid Method [23–27]

which permits to impose the sharp jump conditions across the interface required to simulate two phase flows with phase change [28–33]. Specifically, the Ghost Fluid Thermal Solver for Boiling (GFTSB) presented in [34] is used for the computation of the heat transfer and phase change. Indeed, the liquid and gaseous temperature fields are solved, imposing $T_l = T_{sat}$ and $T_v = T_{sat}$ at the interface. In order to improve the temperature gradients evaluations at the interface, the temperature fields are extended across the
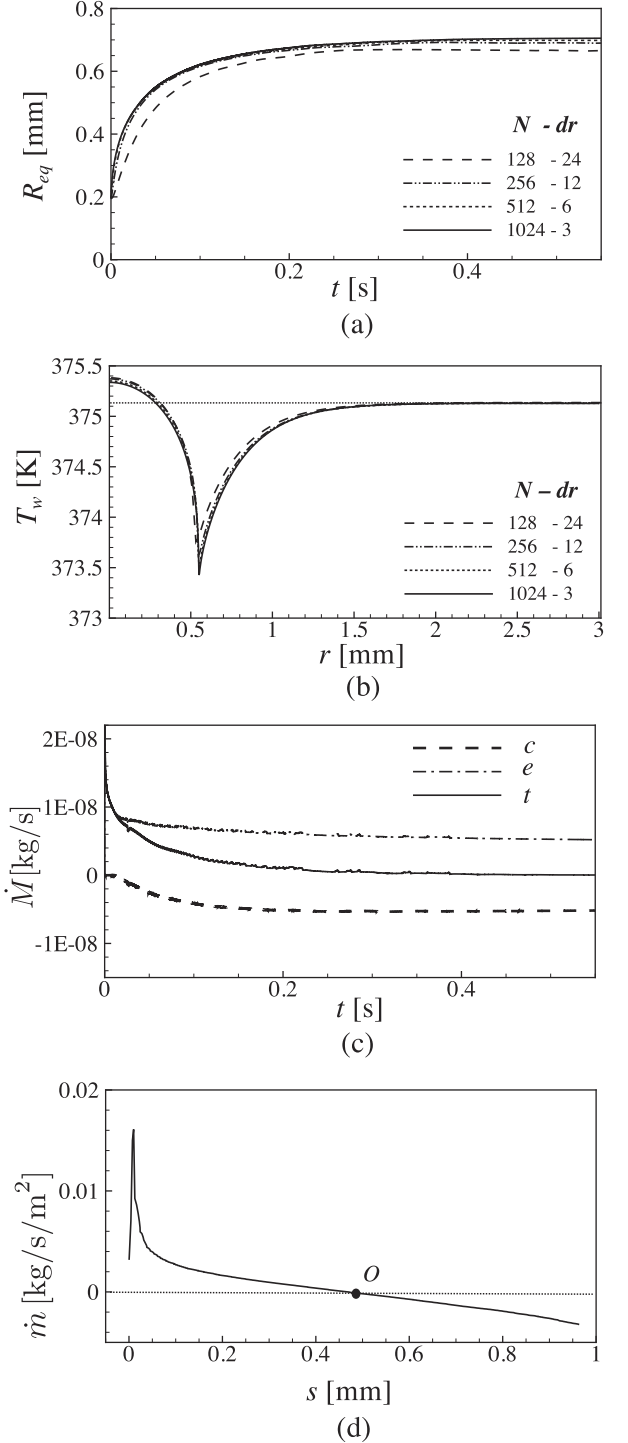

Fig. 3. Results for $Ja_c/Ja_e = 5$ and $\theta_a = 50°$. Temporal evolutions of the equivalent vapour radius (a) and spatial distribution of temperature along the wall ($z = 0$) (b) for different grids (dr in μm). Temporal evolution of the phase change mass flow rate (c) and distribution of the specific phase change mass flow rate along the bubble interface s (curvilinear abscissa) (d).
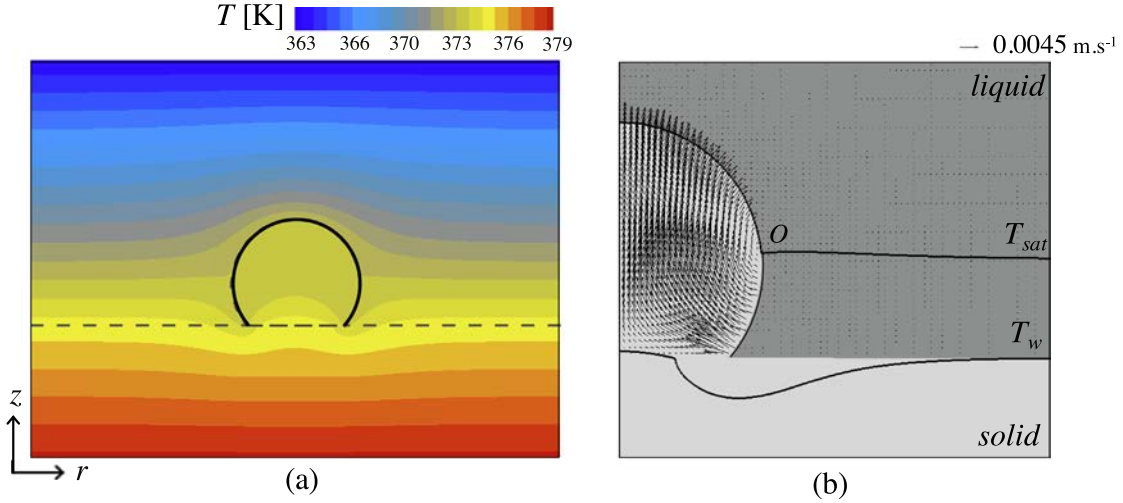
Fig. 4. Stationary fields for $Ja_c/Ja_e = 5$, $\theta_a = 50°$. (a) Temperature field in the fluid and in the solid. Solid line: bubble interface. Dashed line: wall. (b) Velocity field vectors and isothermal lines for $T = T_{sat}$ (black) and $T = T_{w,i}$ (grey).

interface with second order extrapolations [35,31]. The vapour generation $\dot{m}$ is then computed according to Eq. (15). The pressure Poisson equation (resulting from the projection method) is solved with a Black-Box MultiGrid Solver [36]. Fifth order WENO-Z schemes are used for the convective terms [37], second order finite differences for the diffusion terms, and a second order Runge Kutta scheme for the temporal integration. In addition, at each time step, the resolution of the thermal field in the solid wall and of the conservation laws in the fluid are coupled by imposing the appropriate boundary conditions at the solid/fluid interface. The solver has been previously validated by comparisons with experimental data of two phase flows in both isothermal conditions in normal gravity [38,39] and micro-gravity conditions [40,41], and with phase change, for nucleate boiling [42] and also for impacting droplets in the Leidenfrost regime [43]. Moreover, a comparison between numerical results and analytical model for droplet condensation has recently been carried out [44].

The MPI libraries are implemented in order to parallelise the solver: the computations presented in this work have been carried out using from 64 to 256 processors in parallel.

4. Numerical simulation of a bubble nucleated in zero gravity conditions

The axisymmetric configuration selected in this study includes a cylindrical domain of radius L_r and height L_z for the fluid and is depicted in Fig. 2. The radial and axial dimensions are equal, $L_r = L_z = L$, and L = 3 mm. The thickness of the solid wall is $L_w = L/2$. Fluid properties are those of water H_2O and the solid properties are similar to those of a plastic material. The thermophysical properties for $p = 1.01$ bar are summarised in Table 1.

Two isothermal boundary conditions are imposed: free outlet with $T = T_{sub}$ at $z = L$ for the fluid, and a $T = T_o$ at $z = -L/2$ for the solid. The wall at $r = L$ is adiabatic since we assume that in the far field only longitudinal variations (z direction) of the temperature may occur. A symmetry condition is inferred in $r = 0$. At the solid/fluid interface, an equality of the heat fluxes on the fluid and solid sides and a continuity condition for the temperature are imposed. Linear temperature profiles between T_o and $T_{w,i}$ and between $T_{w,i}$ and T_{sub} are used as initial conditions, where $T_{w,i}$ is the initial wall temperature at the solid-fluid interface ($z = 0$). The initial temperature field is shown in Fig. 2. Specifically, for a given couple of temperatures T_{sub} and $T_{w,i}$, T_o is evaluated in order to have an initial constant heat flux over the entire domain, thus verifying:

$$k_l \frac{T_{w,i} - T_{sub}}{L} = k_w \frac{T_o - T_{w,i}}{L/2}. \tag{17}$$

A vapour seed is initially deposited at the wall at $r = 0$. The seed has a circular shape, of radius 200 μm, shifted upward in order to form the desired contact angle as shown in Fig. 2. The apparent contact angle θ_a is then imposed with a condition on the level set function at $z = 0$ (i.e. we do not simulate the micro-region, see the appendix in [19] for more details), and is kept constant all over the simulation time. Note that size of the initial vapour seed will only impact the initial dynamics of the bubble but it is not expected to have any consequence on the equilibrium radius, that will be reached in stationary conditions. This point has been verified numerically, carrying out the same simulation with smaller initial seeds, and checking that the same equilibrium radius is reached.

As a first test case, a Jakob numbers ratio of $Ja_c/Ja_e = 5$ is considered ($T_w = T_{sat} + 2$ K and $T_{sub} = T_{sat} - 10$ K) with $\theta_a = 50°$. The same computation has been carried out with four different uniform cartesian meshes having a number of cells N of 128^2, 256^2, 512^2 and 1024^2 in the fluid domain, corresponding to cell sizes dr ($= dz$) varying from 24 to 3 microns. The same size for the cells is used in the solid domain which measures half the height of the fluid, and thus the solid grid contains $N/2$ cells. The temporal evolution of the equivalent radius of the bubble R_{eq}[1] is shown in Fig. 3(a) for the different grids, until the stationary conditions are reached, around $t = 0.5$ s. At that time, in Fig. 3(b) are reported the radial distributions of the wall temperature ($z = 0$), and the initial wall temperature $T_{w,i} = 375.12$ K is also reported for comparison (clear dashed line). The convergence of the results is emphasised by these curves and we can conclude that cell sizes smaller or equal to 3 μm are required in order to simulate the subtle equilibrium between evaporation and condensation that characterises stationary conditions. Note that, we are assuming that in these conditions there is no micro-layer under the bubble in stationary conditions which indeed would have required finer grid, smaller than the micron, in order to be simulated. This assumption is in agreement with recently

---

[1] The equivalent radius R_{eq} is the radius of a spherical bubble having a volume equal to the volume of vapour $\mathcal{V}_v : R_{eq} = (3\mathcal{V}_v/(4\pi))^{1/3}$.
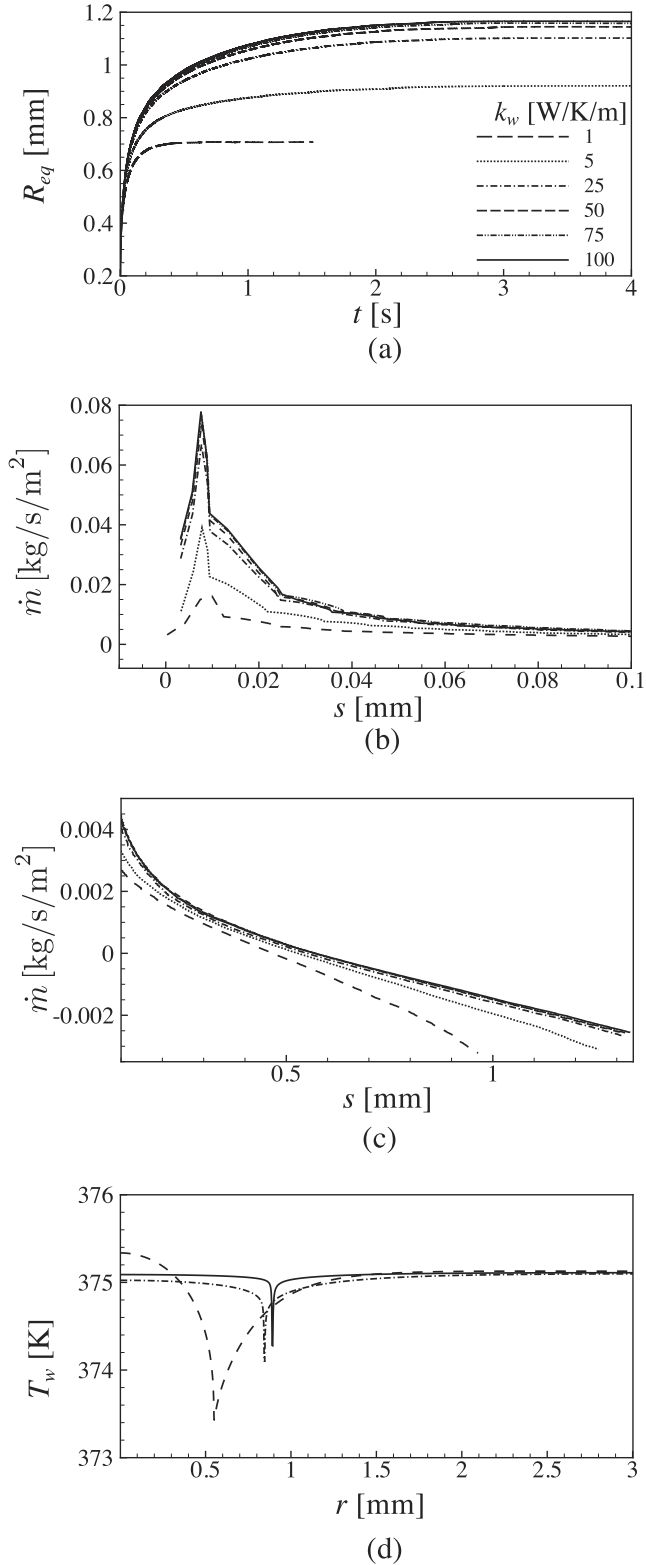
Fig. 6. (a) Equivalent bubble radius for different L. (b) Dimensionless equivalent radius against a reduced time, computed with different L.

Fig. 7. Temporal evolution of R_{eq} varying T_{sub} and T_w for a same $Ja_c/Ja_e = 5$.

Fig. 5. Numerical results for $Ja_c/Ja_e = 5$ and $\theta_a = 50°$ for different k_w. (a) Equivalent diameter of the bubble against time. (b) and (c) $\dot{m}$ distribution along the bubble interface in stationary conditions. (d) T_w distribution ($y = 0$) in stationary conditions.

published works [45,46,19] where it is demonstrated that the micro-layer formation and depletion are dynamic phenomena affecting the first part of the bubble growth only. Therefore, the existence of a micro-layer in the present configuration could maybe affect the tran-
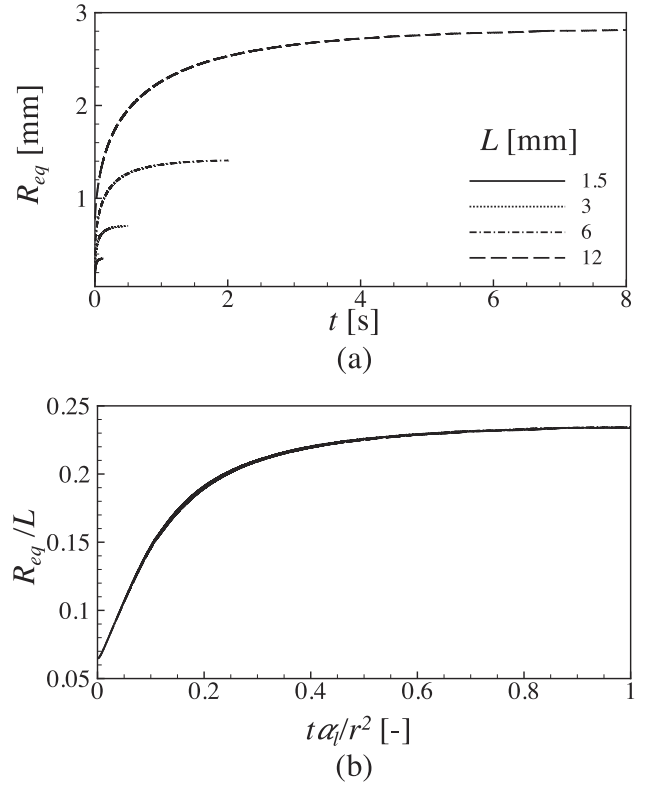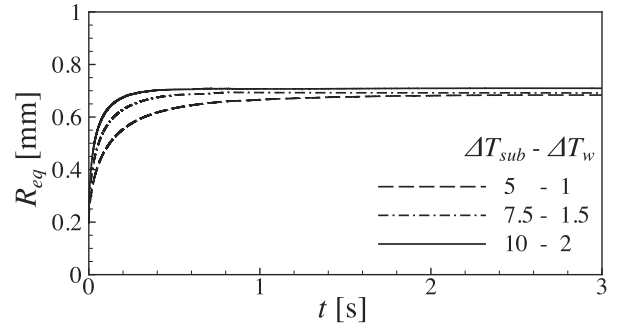
sitory behaviour of the bubble, but the micro-layer will be anyway depleted before a stationary equilibrium is reached. All the results presented in the rest of the work have been obtained using a grid of 1024^2 cells for the fluid domain (i.e. $dr = 3\,\mu m$).

In Fig. 3(c) are shown the temporal evolutions of the mass flow rates of phase change integrated over the bubble surface: $\dot{M}_e$ is the mass flow rate of evaporation ($\dot{M}_e > 0$), $\dot{M}_c$ is the mass flow rate of condensation ($\dot{M}_c < 0$) and $\dot{M}_t$ is their sum. Initially, there is only evaporation ($\dot{M}_c = 0$), until the bubble grows enough to reach the subcooled region and the growth of bubble slows down. Eventually, the stationary conditions are reached when evaporation and condensation compensate each other and $\dot{M}_t$ tends toward a zero value.

The temperature field obtained in stationary conditions for this case can be observed in Fig. 4. The temperature field is perturbed by the presence of the bubble both in the liquid and in the solid. In particular, we can see the presence of a cold region in the solid,

in the neighbourhood of the contact line. This was expected and has been observed also in Fig. 3(b) where the wall temperature shows clearly a drop at the contact line. The results in this region, where the evaporation is the strongest, are very sensitive to the properties of the conductive wall, and special attention will be given to this aspect in the next section. In Fig. 4(b) the velocity vectors field can be observed, and the bubble interface is identified with the thick black line. Two isothermal lines are also reported: the saturation temperature T_{sat} in black and the initial wall temperature $T_{w,i}$ in grey. The saturation isothermal line intercepts the bubble interface (which is at T_{sat}) perpendicularly in a point O. Therefore, in this point, the normal temperature gradient is zero and so is the phase change mass flow rate. As demonstrated by the velocity vectors, the O point delimitates the upper part of the bubble which condensates (mass flow rate leaving the bubble, outward vectors) from the downward part which is inflated by the liquid evaporation (mass flow rate entering the bubble, inward vectors). The point O is highlighted also in Fig. 3(d) and corresponds to the point at which the specific mass flow rate $\dot{m}$, which is reported along the interface, reaches a zero value. The curvilinear abscissa s in this figure indicates the path along the interface, starting at the contact line and ending at the top of the bubble (symmetry axis). It

is interesting to see how the maximum $\dot{m}$ is not reached at the contact line but at a slightly higher s position. Actually, at the contact line the temperature is T_{sat} and in the nearby solid region the temperature drops (as seen in Fig. 4) and this eventually induces a decrease of the mass flow rate of evaporation phase change.

4.1. Influence of the wall conductivity

As noticed by the previous analysis of Fig. 4, the temperature field in the solid is strongly influenced by the nucleate boiling and nucleate boiling is affected by the wall heat conduction. In particular for zero gravity conditions, where stationary equilibrium situations are reached, the thermal equilibrium around the contact line strongly impacts all the problem [47,2]. This is why the numerical resolution of a coupled problem (conduction in the solid and two-phase flow) is mandatory. However, this also means that the selection of a specific solid material affects the solution. Specifically, the previous results have been obtained for a low thermal conductive material: $k_w = 1$ W/K/m. To understand the importance of the wall conductivity on the results, the same case ($Ja_c/Ja_e = 5$ and $\theta_a = 50°$) has been simulated varying k_w from 1 up to 100 W/K/m, and the results are shown in Fig. 5, in terms of equivalent
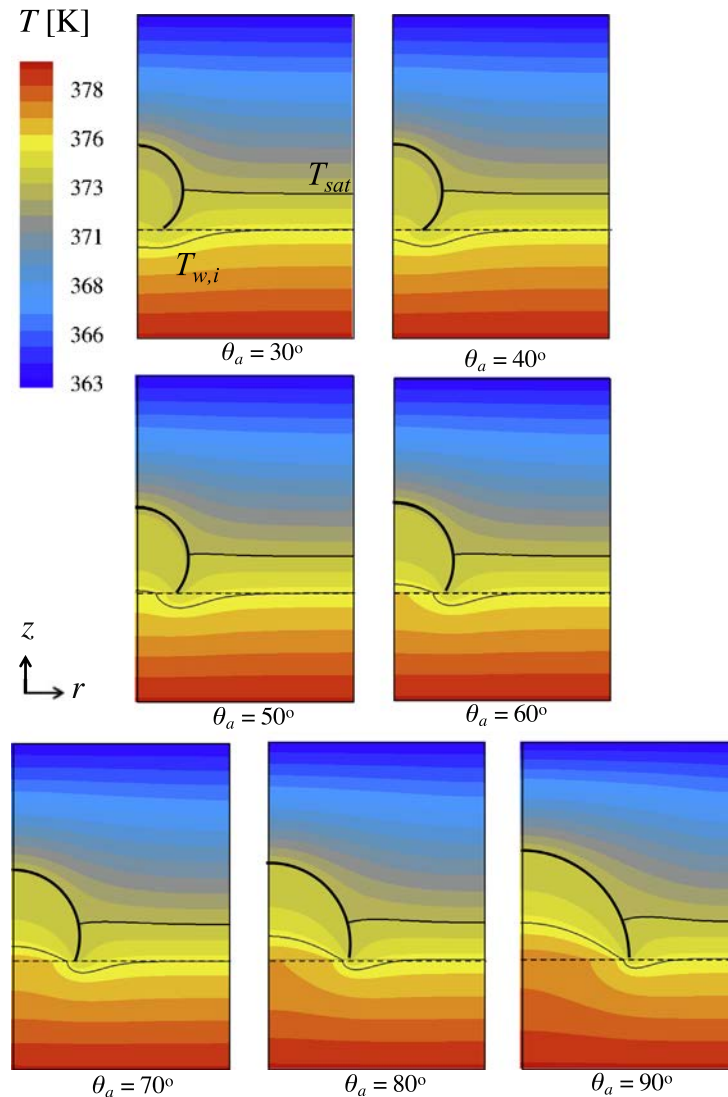

Fig. 8. Temperature fields in the fluid and solid domains for different contact angles θ_a and $Ja_c/Ja_e = 5$. Thick black line: bubble interface. Dashed line: wall. Isothermal lines: $T = T_{sat}$, black, $T = T_{w,i} = 375.12$ K, grey.

bubble radius (a), mass flow rate profile along the bubble interface, (b) near the wall and (c) for higher s, and wall temperature distribution (d). One can observe in this figure that the cold region extent decreases if the wall thermal conductivity increases. As a consequence, the peak in the evaporative mass flow rate is more important for higher k_w (see Fig. 5(b)) and the equilibrium radius of the bubble increases. In fact, the bubble has to grow more in order to increase the condensation mass flow rate and to compensate the evaporative mass flow rate. This is visible in Fig. 5(c) where it appears that if k_w increases the extension of the interface where condensation occurs ($\dot{m} < 0$) increases. This suggests a dependence of the equilibrium diameter over the ratio k_w/k_l. It appears that the differences varying k_w are greater for small k_w and that the results tend to an asymptotic value for high k_w. However, additional simulations with more refined grids are required to strengthen these observations. In fact, a higher wall thermal conductivity involves a higher thermal gradient in the vicinity of the contact line. Cell sizes smaller than 1 μm would have been necessary in order to fit with the thinner region in the solid near the contact line where the temperature strongly varies.

These results show that for small k_w/k_l the solid wall at the contact line tends to acquire the interface temperature which does not change ($T_\Gamma = T_{sat}$ at $p = 1.01$ bar), as assumed in our model (see Section 3.1). The results converge for $k_w \simeq k_l$, which indicates that the assumption of a constant interface temperature is justified in these conditions. However, this is not the case for higher k_w/k_l ratios, for which the results do not converge. In agreement with the model proposed by Nikolayev for the micro-region in proximity of the contact line [48], we can speculate that when k_w/k_l is high, the wall keeps its temperature, and the interface temperature increases in order to obtain a thermal equilibrium at the contact line. This eventually leds to a local variation of the pressure jump and curvature. We cannot describe such phenomena with the employed models and mesh refinements. Therefore, the above comments for high k_w/k_l remain qualitative and need to be confirmed by future works. Consequently, the following study has been carried out with $k_w = 1$ W/K/m ($k_w/k_l = 1.5$), for which space convergence has been demonstrated previously.

4.2. Influence of the height of the domain, L

The analytical model that has been established in Section 2 indicates a proportionality between the equilibrium radius and the domain height L. This proportionality is related to the temperature gradient induced by the temperatures enforced at the domain borders. Indeed, increasing L keeping constant T_{sub} and T_w means decreasing the thermal gradient. As a consequence, our model predicts a linear increase of the equilibrium bubble diameter with L. To verify if this assumption is correct, the previous test case (same T_w and T_{sub}, $Ja_c/Ja_e = 5$ and $\theta_a = 50°$) has been carried out with $L = 1.5$ mm, $L = 6$ mm and $L = 12$ mm (in addition to the $L = 3$ mm case). The temporal evolutions of R_{eq} are shown in Fig. 6(a). In Fig. 6(b) dimensionless curves have been plotted with the expected scaling. The relevance of the scaling is demonstrated since all the curves collapse on one single curve of R_{eq}/L as a function of a reduced time $t\alpha_l/R_{eq}^2$, where α_l is the thermal diffusivity of the liquid (which is the same in all the computations). The simulations that will be presented in the rest of the paper have been carried out using a domain with $L = 3$ mm, but this analysis will permit to extend the results to a generic L.

4.3. Influence of the temperatures

The analytical model of Eq. (8) only indicates that varying T_w and T_{sub} but keeping constant the ratio Ja_c/Ja_e the equilibrium

radius should remain unchanged. To verify this assumption, two simulations have been carried out, keeping the same $Ja_c/Ja_e = 5$ (and the same $\theta_a = 50°$) as the reference case but changing the temperatures: $T_{sat} - T_{sub} = 5/7.5$ K and $T_w - T_{sat} = 1/2$ K. The results, which are shown in Fig. 7, indicate that the temperatures impact the transitory behaviour but that the stationary equilibrium radius is the same with a precision of 3%. More specifically,
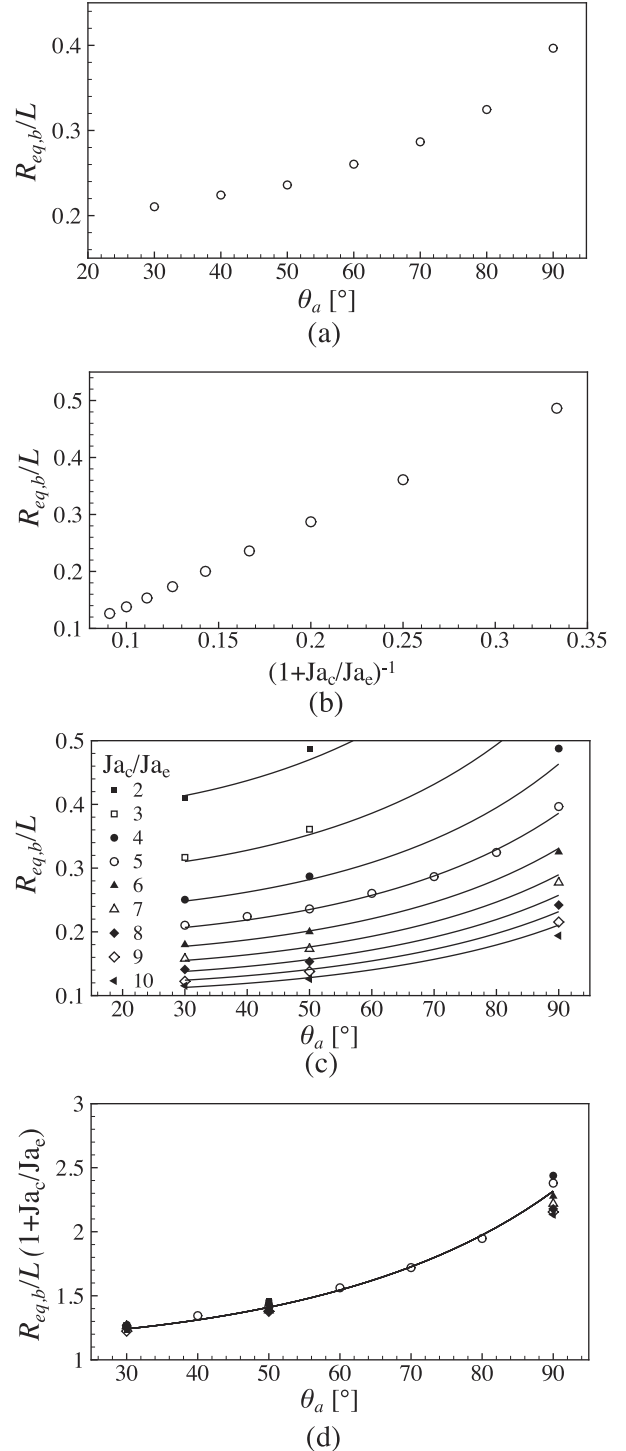

Fig. 9. (a) Dimensionless equivalent radius at equilibrium $R_{eq,b}/L$ obtained with $Ja_c/Ja_e = 5$ against θ_a. (b) $R_{eq,b}/L$ obtained with different Ja_c/Ja_e for $\theta_a = 50°$. (c) and (d) Comparisons between numerical results (symbols) and the analytical model Eq. (18) (solid line).

we observe that increasing T_w the initial speed of growth of the bubble is higher and eventually the stationary condition is reached faster.

5. Numerical correlation for the equilibrium radius

We present in this section simulations of nucleate boiling in zero gravity conditions in order to compare the previously developed model and the numerical results. A parametric study has been carried out varying the contact angle θ_a and the ratio Ja_c/Ja_e. The contact angle influence can be observed in Fig. 8 where results corresponding to $Ja_c/Ja_e = 5$, and θ_a varying between 30° and 90° in stationary conditions at $t = 1$ s are reported. The bubble interface is drawn with a thick black line and the wall is represented with a dashed line. Two isothermal levels are emphasised: $T = T_{sat}$ in black and $T = T_{w,i}$ in grey. It appears that increasing θ_a, both the equilibrium radius and the bubble influence region enlarge. Moreover, the surface of the dry region under the bubble and the temperature in that region increase. The consequence will be an impact on the heat transfer that will be analysed in Section 6. The dimensionless equivalent radius of the bubble at equilibrium $R_{eq,b}/L$ is shown against θ_a in Fig. 9(a). Similar simulations have

been carried out for Ja_c/Ja_e between 2 and 10, for 3 angles: 30°, 50°, et 90°. Results are shown in Fig. 9(b) for $\theta_a = 50$°: we see that the radius increases linearly with $(1 + Ja_c/Ja_e)^{-1}$ in agreement with Eq. (8).

Finally, all the results are summarised in Fig. 9(c), with symbols. In order to fit the numerical results for the equivalent bubble radius, a multiplier $C = 1.15829$ is used in Eq. (8) to get the following correlation:

$$\frac{R_{eq,b}}{L} = C\left[\left(1 + \frac{Ja_c}{Ja_e}\right) \cos\theta_a + \frac{\sin^2\theta_a}{2(1 + \cos\theta_a)}\right]^{-1}. \quad (18)$$

The evolutions calculated with Eq. (18) are represented with solid lines and compared to numerical results in Fig. 9(c) and (d).

Note that, the original analytical model established in Section 2 gives the bubble equilibrium radius R_b, which, from a geometrical point of view, is the radius of a partial sphere (see Fig. 1). However, the numerical results have shown that the equivalent bubble radius $R_{eq,b}$ indeed follows this correlation. In order to obtain a correlation for R_b, Eq. (18) must be multiplied by the ratio between the radii of the partial and equivalent spheres, which is a function of θ_a only (see Appendix B for more details). In conclusion, according to
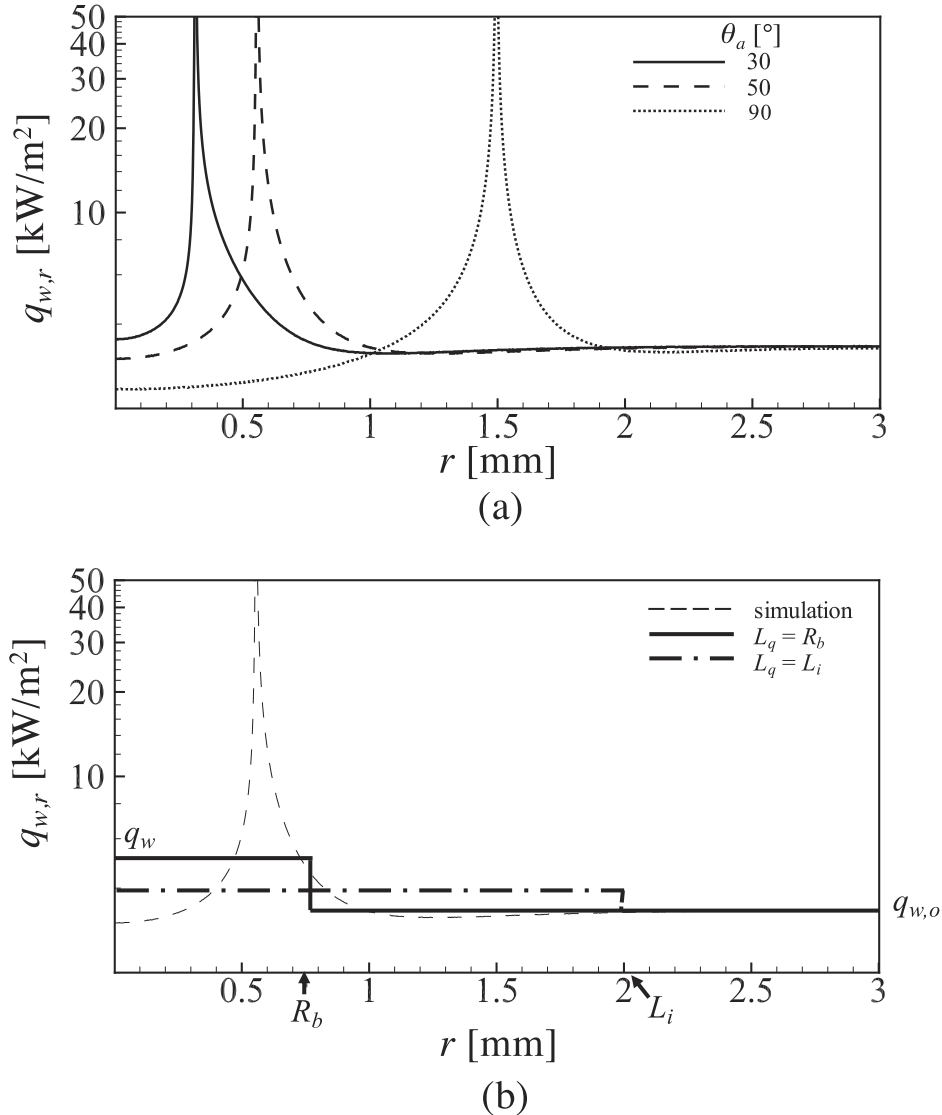

(a)

(b)

Fig. 10. Distributions of the local heat flux (log scale). (a) $q_{w,r}$ in the numerical simulations for $Ja_c/Ja_e = 5$. (b) Schematic of $q_{w,r}$ evaluated from the model of Eq. (21) for different normalisation length L_q choices.

our numerical results, the correlation for the equilibrium radius R_b is:

$$\frac{R_b}{L} = C \left[\left(1 + \frac{Ja_c}{Ja_e} \right) \left(\cos\theta_a + \frac{\sin^2\theta_a}{2(1+\cos\theta_a)} \right) \right]^{-1}$$
$$\times \left(\frac{4}{4 - (2+\cos\theta_a)(1-\cos\theta_a)^2} \right)^{1/3}. \quad (19)$$

The average error between correlation and data is 1.3%, and a maximum error of 7% is reached for angles $\theta_a = 90^o$. We could expect that the analytical model, which does not consider the impact of the bubble on the thermal field, departs from the numerical results at high angles for which indeed the thermal field is more affected by the presence of the bubble (as was observed in Fig. 8). As commented in Section 4.1, the equilibrium radius is strongly affected by the wall conductivity. Therefore, we can expect the multiplier C to be a function of the ratio k_w/k_l. The establishment of the dependence $C(k_w/k_l)$ will be the purpose of future works.

6. Parametric analysis of the heat transfer behaviour

The wall heat transfer is strongly affected by nucleate boiling, as can be qualitatively observed in the temperature field of Fig. 8. The radial evolution of local heat flux $q_{w,r}$ is reported in Fig. 10 for $Ja_c/Ja_e = 5$ and three different θ_a. We can observe that the heat flux has a peak at the contact line and then decreases up to a constant value $q_{w,0}$. The $q_{w,0}$ corresponds to the heat flux we would obtain without nucleate boiling $q_{w,0}$ (i.e. if we would have only a superheated liquid):

$$q_{w,0} = k_l \frac{T_{w,i} - T_{sub}}{L_z}. \quad (20)$$

We can estimate an influence length L_i of a bubble by considering the radial coordinate starting from which the local heat flux $q_{w,r}$ is equal to the heat flux without nucleate boiling $q_{w,0}$, with a tolerance of 1%. Graphically, these lengths correspond in Fig. 8 to the abscissa for which the isothermal line $T_{w,i}$ (grey solid line) reaches the wall (dashed line). In Fig. 10(a) they correspond to the abscissa for which $q_{w,r}$ reaches the constant plateau of value $q_{w,0}$. From Fig. 10 we observe that the influence of the bubble on the heat transfer is significant both in the region under the bubble, at the contact line region and up to L_i.

The numerical simulations data are used in order to evaluate the Nusselt number, Nu, for each case. To do so, we express $q_{w,r}$ with a piece-wise distribution: $q_{w,r} = q_w$ for $r < L_q$ and $q_{w,r} = q_{w,0}$ for $L_q < r < L_r$. The length L_q is a normalisation length, with $L_q < L_r$. The value of q_w is calculated ensuring that for a given choice of L_q the integrated heat flux Q_{tot} (total power in W) is the same, according to the following equation:

$$Q_{tot} = q_w \pi L_q^2 + q_{w,0} \pi \left(L_r^2 - L_q^2 \right), \quad (21)$$

and Q_{tot} is calculated form the numerical results taken in stationary conditions with the following integral:

$$Q_{tot} = \int_0^{L_r} k \frac{dT}{dz} \Big|_w 2\pi r dr. \quad (22)$$

Note that in the present work $L_r = L_z = L$. We consider a Nu based on the ratio between the heat flux q_w calculated with Eq. (21) and $q_{w,0}$:

$$Nu = \frac{q_w}{q_{w,0}}. \quad (23)$$

For the normalisation length L_q two choices could be convenient: L_i or R_b. The corresponding piece-wise distributions of $q_{w,r}$ are schematically reported in Fig. 10 (b) for $Ja_c/Ja_e = 5$ and $\theta_a = 50°$. Choosing R_b as a normalisation length gives a higher q_w than choosing L_i because $R_b < L_i$. However, for both choices, the integral of q_w over the domain will be the same, according to Eq. (21). The drawback in choosing L_i is that it is evaluated on the basis of a tolerance criteria, and therefore contains the error associated with the tolerance. On the other hand, R_b comes from the position of the bubble
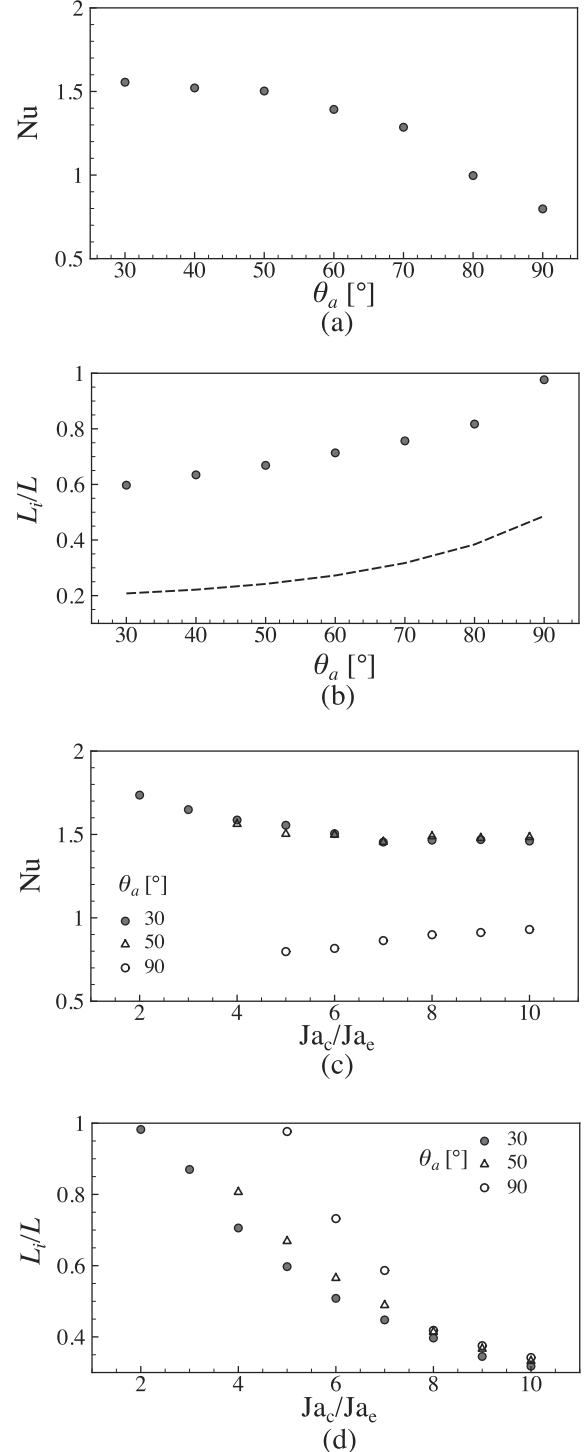

Fig. 11. Nusselt number Nu (a), dimensionless influence length L_i/L (symbols) and R_b/L (dashed line) (b) for $Ja_c/Ja_e = 5$ as function of θ_a. Nu (c) and L_i/L (d) for different θ_a as a function of Ja_c/Ja_e.

interface and is therefore more precise. Moreover, a correlation Eq. (19) has been established for R_b. Eventually the choice $L_q = R_b$ has been made in the present work. However, note that the following simple relation exists between a Nu_{R_b} and Nu_{L_i}, evaluated respectively with $L_q = R_b$ and $L_q = L_i$:

$$\frac{Nu_{L_i} - 1}{Nu_{R_b} - 1} = \frac{L_i^2}{R_b^2}. \tag{24}$$

In the rest of the paper Nu indicates Nu_{R_b}.

The Nu evolution with θ_a is reported in Fig. 11(a) for the case $Ja_c/Ja_e = 5$. We see that the Nu is around 1.5 for θ_a up to 50°, which indicates that in these conditions the heat transfer is enhanced thanks to the phase change. For higher contact angles, the Nusselt number decreases and reaches values smaller than one for angles greater than 80°. The ratio L_i/L for $Ja_c/Ja_e = 5$ is reported in Fig. 11(b) for different θ_a and the R_b/L evolution is reported for comparison. It appears that increasing θ_a, the length L_i enlarges for the case $Ja_c/Ja_e = 5$. The extent of the dry zone, characterised by a low heat transfer capacity, also becomes larger and ends up to compensate or eventually to overcome the heat transfer enhancement induced by the phase change. This can be deduced also from Fig. 10(a) which shows that $q_{w,r} < q_{w,0}$ under the bubble and it decreases when θ_a increases. We find the same behaviour also for the other ratios Ja_c/Ja_e for which the Nu and L_i are reported in Fig. 11(c) and (d) respectively for the three θ_a, 30°, 50° and 90°. We see that increasing Ja_c/Ja_e, the Nu decreases for $\theta_a = 30°$ and 50°, while it increases for $\theta_a = 90°$. In fact, for the smaller angles, the phase change is the predominant effect on the heat transfer enhancement and this effect decreases for higher Ja_c/Ja_e because R_b and L_i are smaller. On the contrary, for greater angles, higher Ja_c/Ja_e will induce smaller dry zones and so a lower impact of the dry zone on the Nusselt number.

From a practical point of view, these informations can be useful in determining the heat transfer expected throg a surface with nucleate boiling in zero gravity conditions. Indeed, from the Ja_c/Ja_e and θ_a the equilibrium radius R_b can be estimated from Eq. (19) and the corresponding Nusselt number can be extracted from Fig. 11. Finally, the total heat Q transferred throw a surface $\mathcal{A}$ with N nucleation sites can be evaluated from the following equation:

$$Q = N\,Nu\,q_{w,0}\,\pi R_b^2 + q_{w,0}\left(\mathcal{A} - N\pi R_b^2\right), \tag{25}$$

with Q in Watt, and N without dimension. Equivalently Eq. (25) can be arranged in the following form:

$$Q = N q_{w,0} \pi R_b^2 (Nu - 1) + q_{w,0}\,\mathcal{A}, \tag{26}$$

which shows that when $Nu > 1$ the heat transfer is enhanced with respect to the case without nucleate boiling: $Q > q_{w,0}\mathcal{A}$. On the contrary if $Nu < 1$ the heat transfer is deteriorated: $Q < q_{w,0}\mathcal{A}$.

7. Conclusion

Direct numerical simulations of nucleate pool boiling of partly sub-cooled liquids over superheated walls, in zero gravity conditions, have been carried out and analysed in this work. A coupled numerical simulation of the two phase flow and the heat conduction in the solid has permitted to carry out highly accurate conjugate heat transfer simulations. Actually, the results have highlighted that the impact of the heat conduction in the wall in these configurations is of primary importance. Indeed, the equilibrium radius is reached in these configurations when the mass flow rate of phase change associated with condensation and evaporation compensate each other. However, the greater part of the evaporation mass flow rate is concentrated in a small region near the contact line. Therefore, the wall temperature change in the neigh-

bourhoods of the contact line, induced by modifications in the heat transfer capacities in the solid for instance, strongly influences the evaporation mass flow rate and hence the equilibrium radius. Very refined simulations enabled us to observe that for low ratios k_w/k_l the heat flux at the contact line tends to zero locally at very low scale. This can be explained by considering the thermal equilibrium that occurs between the interface and the solid wall. As expected the local heat flux strongly increases while going away from the contact line and then decreases along the interface at larger distances from the wall. A parametric study has been carried out varying the sub-cooling and the overheat, that is the Jakob numbers of condensation and evaporation, as well as the contact angle. Starting from an analytical model, based on the equilibrium between the mass flows of phase change, corrected with a multiplier on the basis of the numerical results, a correlation of the dimensionless radius has been established. This correlation shows that it exists an inverse proportionality between the equilibrium radius and the temperature gradient. Moreover, the dimensionless radius R_b/L increases when Ja_c/Ja_e decreases and when θ_a increases. Finally, the impact of the parameters on the heat transfer has been investigated. Nu numbers, with reference surfaces equal to the bubble shades on the wall (circles of radius R_b) have been evaluated. Their analysis shows an enhancement of the heat transfer ($Nu > 1$) at small angles, with a Nu that decreases when Ja_c/Ja_e increases. On the other hand, for angles greater than 80° the heat transfer is deteriorated ($Nu < 1$), but the Nu increases with the ratio Ja_c/Ja_e. The joint utilisations of the equilibrium radius and of the Nu numbers can be used in order to evaluate the expected heat fluxes in nucleate pool boiling in zero gravity conditions.

Declaration of Competing Interest

The authors declared that there is no conflict of interest.

Acknowledgements

Appendix A. Complementary material for the analytical model

In this appendix are reported some complementary passages that have permit to obtain the analytical model for the equilibrium radius Eq. (8). The unperturbed temperature field $T(z)$ is given by Eq. (1). The tangential coordinate θ of the spherical reference frame is related to the z coordinate of the cylindrical reference frame by the relation (see Fig. 1):

$$z = R\cos\theta_a + R\sin\theta, \tag{A.1}$$

which, when replaced in Eq. (8), permits to obtain Eq. (6). The temperature normal gradient across the thermal boundary layer of thickness δ, evaluated in a point (R, θ) along the interface, is given by:

$$\nabla T_l \cdot \vec{n} = \frac{\partial T}{\partial r} n_r + \frac{\partial T}{\partial z} n_z, \tag{A.2}$$

$$= \frac{T(\theta) - T_{sat}}{\delta_r} n_r + \frac{T(\theta) - T_{sat}}{\delta_z} n_z, \tag{A.3}$$

where the have assumed $\delta/R \ll 1$. In Eq. (A.3), $n_r = \cos\theta$ and $n_z = \sin\theta$ are the normal vector components in the r and z directions. The thermal boundary layer thickness δ is also decomposed in r and z components: $\delta_r = \delta/\cos\theta$ and $\delta_z = \delta/\sin\theta$, and replacing in Eq. (A.3) the temperature normal gradient can be expressed with Eq. (7). Combining Eqs. (7), (6) and (5) simplifying, the following equation to be solved for the equilibrium radius $R = R_b$ is found:

$$\int_{-\frac{\pi}{2}+\theta_a}^{\frac{\pi}{2}} \left(T_w + \frac{T_{sub} - T_w}{L}(R\cos\theta_a + R\sin\theta) - T_{sat} \right) \cos\theta\, d\theta = 0. \tag{A.4}$$

Solving the integral and applying some basic trigonometric formula the following expression for R_b/L is obtained:

$$\frac{R_b}{L} = \frac{T_w - T_{sat}}{T_w - T_{sub}} \left(\frac{1 + \cos\theta_a}{\cos\theta_a(1 + \cos\theta_a) + \frac{1}{2}\sin^2\theta_a} \right). \tag{A.5}$$

The Jakob numbers of condensation Ja_c and evaporation Ja_e for the bubble are defined by:

$$Ja_e = \frac{c_{pl}(T_w - T_{sat})}{L_{vap}}, \qquad Ja_c = \frac{c_{pl}(T_{sat} - T_{sub})}{L_{vap}}. \tag{A.6}$$

Therefore the ratio of the temperature sub-cooling and overheat corresponds to the Jakob ratio, as expressed by Eq. (9), which can be used in Eq. (A.5) to get the final expression for the equilibrium radius Eq. (8).

Appendix B. Relation between $R_{eq,b}$ and R_b

In zero gravity condition, the equilibrium shape of a bubble with a contact angle θ_a is a partial sphere of radius R_b having a volume $\mathcal{V}_b$ given by:

$$\mathcal{V}_b = \frac{4}{3}\pi R_b^3 - \frac{\pi}{3}R_b^3(2 + \cos\theta_a)(1 - \cos\theta_a), \tag{B.1}$$

as schematically depicted in Fig. 1. The equivalent radius of the bubble $R_{eq,b}$ is the radius of a spherical bubble having a volume equal to $\mathcal{V}_b$, thus verifying:

$$\mathcal{V}_b = \frac{4}{3}\pi R_{eq,b}^3. \tag{B.2}$$

Using Eq. (B.1) and Eq. (B.2), the radius of the bubble R_b can be expressed as a function of the equivalent radius $R_{eq,b}$:

$$R_b = R_{eq,b} \left(\frac{4}{4 - (2 + \cos\theta_a)(1 - \cos\theta_a)^2} \right)^{1/3}. \tag{B.3}$$

References

[1] C. Colin, O. Kannengieser, W. Bergez, M. Lebon, J. Sebilleau, M. Sagan, S. Tanguy, Nucleate pool boiling in microgravity: Recent progress and future prospects, Comptes Rendus Mecanique 345 (2017) 21–34.

[2] E. Wagner, C. Sodtke, N. Schweizer, P. Stephan, Experimental study of nucleate boiling heat transfer under low gravity conditions using tlcs for high resolution temperature measurements, Heat Mass Trans. 42 (2006) 875–883.

[3] G.R. Warrier, V.K. Dhir, D.F. Chao, Nucleate pool boiling experiment (npbx) in microgravity: International space station, Int. J. Heat Mass Transf. 83 (2015) 781–798.

[4] X. Ma, P. Cheng, S. Gong, X. Quan, Mesoscale simulations of saturated pool boiling heat transfer under microgravity conditions, Int. J. Heat Mass Transf. 114 (2017) 453–457.

[5] R. Souza, J. Passos, E. Cardoso, Confined and unconfined nucleate boiling under terrestrial and microgravity conditions, Appl. Therm. Eng. 51 (2013) 1290–1296.

[6] D. Serret, D. Brutin, O. Rahli, L. Tadrist, Convective boiling between 2d plates: microgravity influence on bubble growth and detachment, Microgravity Sci. Technol. 22 (2010) 377–385.

[7] J. Straub, Boiling heat transfer and bubble dynamics in microgravity, Adv. Heat Transf. 35 (2001) 57–172.

[8] O. Kannengieser, C. Colin, W. Bergez, Pool boiling with non-condensable gas in microgravity: Results of a sounding rocket experiment, Microgravity Sci. Technol. 22 (2010) 447–454.

[9] J. Kim, J.F. Benton, Highly subcooled pool boiling heat transfer at various gravity levels, Int. J. Heat Fluid Flow 23 (2002) 497–508.

[10] R. Raj, J. Kim, J. McQuillen, Subcooled pool boiling in variable gravity environments, J. Heat Trans. 131 (2009) 091502.

[11] R. Raj, J. Kim, J. McQuillen, Pool boiling heat transfer on the international space station: Experimental results and model verification, Heat Mass Trans. 134 (2012) 101504.

[12] Y. Sato, B. Ničeno, A sharp-interface phase change model for a mass-conservative interface tracking method, J. Comput. Phys. 249 (2013) 127–161.

[13] C. Kunkelmann, P. Stephan, Numerical simulation of the transient heat transfer during nucleate boiling of refrigerant hfe-7100, Int. J. Refrig. 33 (2010) 1221–1228.

[14] S. Gong, P. Cheng, Lattice boltzmann simulation of periodic bubble nucleation, growth and departure from a heated surface in pool boiling, Int. J. Heat Mass Transf. 64 (2013) 122–132.

[15] X. Ma, P. Cheng, 3d simulations of pool boiling above smooth horizontal heated surfaces by a phase-change lattice boltzmann method, Int. J. Heat Mass Transf. 131 (2019) 1095–1108.

[16] E. Aktinol, G.R. Warrier, V.K. Dhir, Single bubble dynamics under microgravity conditions in the presence of dissolved gas in the liquid, Int. J. Heat Mass Transf. 79 (2014) 251–268.

[17] J. Wu, V.K. Dhir, Numerical simulation of dynamics and heat transfer associated with a single bubble in subcooled boiling and in the presence of noncondensables, J. Heat Trans. 133 (2011) 041502.

[18] C.D. Henry, J. Kim, J. McQuillen, Dissolved gas effects on thermocapillary convection during boiling in reduced gravity environments, Heat Mass Trans. 42 (2006) 919–928.

[19] A. Urbano, S. Tanguy, G. Huber, C. Colin, Direct numerical simulation of nucleate boiling in micro-layer regime, Int. J. Heat Mass Transf. 123 (2018) 1128–1137.

[20] D. Juric, G. Tryggvason, Computations of boiling flows, Int. J. Multiphase Flow 24 (1998) 387–410.

[21] S. Osher, J. Sethian, Fronts propagating with curvature-dependent speed: algorithms based on Hamilton–Jacobi formulations, J. Comput. Phys. 79 (1988) 12–49.

[22] M. Sussman, P. Smereka, S. Osher, A level set approach for computing solutions to incompressible two-phase flow, J. Comput. Phys. 114 (1994) 146–159.

[23] R.P. Fedkiw, T. Aslam, B. Merriman, S. Osher, A non-oscillatory eulerian approach to interfaces in multimaterial flows (the ghost fluid method), J. Comput. Phys. 152 (1999) 475–492.

[24] M. Kang, R.P. Fedkiw, X.-D. Liu, A boundary condition capturing method for multiphase incompressible flow, J. Sci. Comput. 15 (2000).

[25] B. Lalanne, L.R. Villegas, S. Tanguy, F. Risso, On the computation of viscous terms for incompressible two-phase flows with level set/ghost fluid method, J. Comput. Phys. 301 (2015) 289–307.

[26] X.-D. Liu, R.P. Fedkiw, M. Kang, A boundary condition capturing method for poisson's equation on irregular domains, J. Comput. Phys. 160 (2000) 151–178.

[27] M. Sussman, K. Smith, M. Hussaini, M. Ohta, R. Zhi-Wei, A sharp interface method for incompressible two-phase flows, J. Comput. Phys. 221 (2007) 469–505.

[28] F. Gibou, L. Chen, D.Q. Nguyen, S. Banerjee, A level set based sharp interface method for the multiphase incompressible navier-stokes equations with phase change, J. Comput. Phys. 222 (2007) 536–555.

[29] F. Gibou, R.P. Fedkiw, L.-T. Cheng, M. Kang, A second-order-accurate symmetric discretization of the poisson equation on irregular domain, J. Comput. Phys. 176 (2002) 2005–2227.

[30] D.Q. Nguyen, R.P. Fedkiw, M. Kang, A boundary condition capturing method for incompressible flame discontinuities, J. Comput. Phys. 172 (2001) 71–98.

[31] S. Tanguy, M. Sagan, B. Lalanne, F. Couderc, C. Colin, Benchmarks and numerical methods for the simulation of boiling flows, J. Comput. Phys. 264 (2014) 1–22.

[32] J. Papac, F. Gibou, C. Ratsch, Efficient symmetric discretization for the poisson, heat and stefan-type problems with robin boundary conditions, J. Comput. Phys. 229 (2010) 875–889.

[33] S. Tanguy, T. Ménard, A. Berlemont, A level set method for vaporizing two-phase flows, J. Comput. Phys. 221 (2007) 837–853.

[34] L. Rueda-Villegas, R. Alis, M. Lepilliez, S. Tanguy, A ghost fluid/level set method for boiling flows and liquid evaporation: application to the leidenfrost effect, J. Comput. Phys. 316 (2016) 789–813.

[35] T.D. Aslam, A partial differential equation approach to multidimensional extrapolation, J. Comput. Phys. 193 (2003) 349–355.

[36] J.E. Dendy, Black box multigrid, J. Comput. Phys. 48 (1982) 366–386.

[37] R. Borges, M. Carmona, B. Costa, W. Don, An improved weighted essentially non-oscillatory scheme for hyperbolic conservation laws, J. Comput. Phys. 227 (2008) 3191–3211.

[38] B. Lalanne, N.A. Chebel, J. Vejražka, S. Tanguy, O. Masbernat, F. Risso, Non-linear shape oscillations of rising drops and bubbles: Experiments and simulations, Phys. Fluids 27 (2015) 123305.

[39] S. Tanguy, A. Berlemont, Application of a level set method for simulation of droplet collisions, Int. J. Multiphase Flow 31 (2005) 1015–1035.

[40] A. Dalmon, M. Lepilliez, S. Tanguy, A. Pedrono, B. Busset, H. Bavestrello, J. Mignot, Direct numerical simulation of a bubble motion in a spherical tank

under external forces and microgravity conditions, J. Fluid Mech. 849 (2018) 467–497.

[41] A. Dalmon, M.L.S. Tanguy, R. Alis, E.R. Popescu, R. Roumiguie, T. Miquel, B. Busset, H. Bavestrello, J. Mignot, Comparison between the fluidics experiment and direct numerical simulations of fluid sloshing in spherical tanks under microgravity conditions, Microgravity Sci. Technol. (2019).

[42] G. Huber, S. Tanguy, M. Sagan, C. Colin, Direct numerical simulation of nucleate pool boiling at large microscopic contact angle and moderate jakob numbers, Int. J. Heat Mass Transf. 113 (2017) 662–682.

[43] L. Rueda-Villegas, S. Tanguy, G. Castanet, O. Caballina, F. Lemoine, Direct numerical simulation of the impact of a droplet onto a hot surface above the leidenfrost temperature, Int. J. Heat Mass Transf. 104 (2017) 1090–1109.

[44] A. Orazzo, S. Tanguy, Direct numerical simulations of droplet condensation, Int. J. Heat Mass Transf. 129 (2019) 432–448.

[45] A. Guion, S. Afkhami, S. Zaleski, J. Buongiorno, Simulations of microlayer formation in nucleate boiling, Int. J. Heat Mass Transf. 127 (2018) 1271–1284.

[46] S. Hänsh, S. Walker, Microlayer formation and depletion beneath growing steam bubbles, Int. J. Multiphase Flow 111 (2019) 241–263.

[47] C. Sodtke, J. Kern, N. Schweizer, P. Stephan, High resolution measurements of wall temperature distribution underneath a single vapour bubble under low gravity conditions, Int. J. Heat Mass Transf. 49 (2006) 1100–1106.

[48] V.S. Nikolayev, Dynamics of the triple contact line on a nonisothermal heater at partial wetting, Phys. Fluids 22 (2010) 082105.